Medical Physics
The International Journal of Medical Physics Research and Practice

Mammogram synthesis using a three-dimensional simulation. III. Modeling and evaluation of the breast ductal network

Predrag R. Bakic, Michael Albert, Dragana Brzakovic, and Andrew D. A. Maidment

Citation: Medical Physics **30**, 1914 (2003); doi: 10.1118/1.1586453
View online: http://dx.doi.org/10.1118/1.1586453
View Table of Contents: http://scitation.aip.org/content/aapm/journal/medphys/30/7?ver=pdfcov
Published by the American Association of Physicists in Medicine

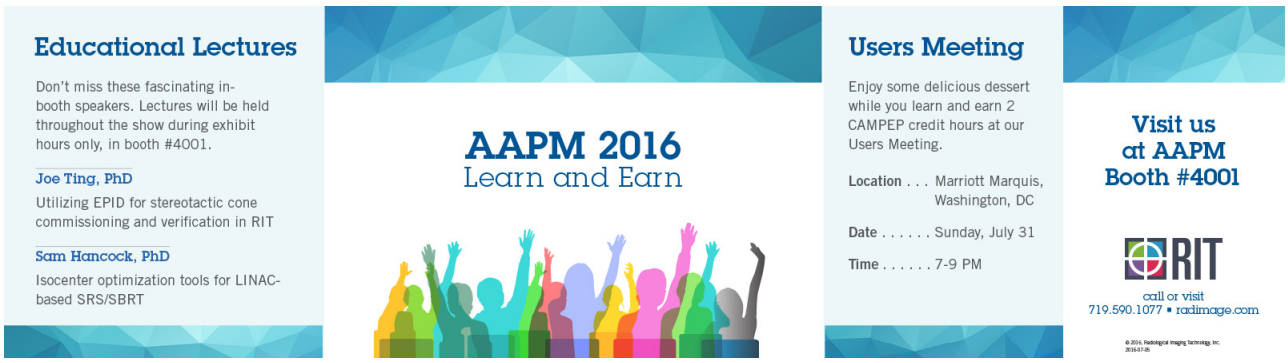

Mammogram synthesis using a three-dimensional simulation. III. Modeling and evaluation of the breast ductal network

Predrag R. Bakic and Michael Albert
Department of Radiology, Hospital of the University of Pennsylvania, 3400 Spruce Street, Philadelphia, Pennsylvania 19104

Dragana Brzakovic
Office of Integrative Activities, National Science Foundation, Arlington, Virginia 22230

Andrew D. A. Maidment[a)]
Department of Radiology, Hospital of the University of Pennsylvania, 3400 Spruce Street, Philadelphia, Pennsylvania 19104

(Received 19 March 2003; revised 2 May 2003; accepted for publication 3 May 2003; published 25 June 2003)

A method is proposed for realistic simulation of the breast ductal network as part of a computer three-dimensional (3-D) breast phantom. The ductal network is simulated using tree models. Synthetic trees are generated based upon a description of ductal branching by ramification matrices (R matrices), whose elements represent the probabilities of branching at various levels of a tree. We simulated the ductal network of the breast, consisting of multiple lobes, by random binary trees (RBT). Each lobe extends from the ampulla and consists of branching ductal segments of decreasing size, and the associated terminal ductal-lobular units. The lobes follow curved paths that project from the nipple toward the chest wall. We have evaluated the RBT model by comparing manually-traced ductal networks from 25 projections of ductal lobes in clinical galactograms and manually-traced networks from 23 projections of synthetic RBTs. A root-mean-square (rms) fractional error of 41%, between the R-matrix elements corresponding to clinical and synthetic images, was computed. This difference was influenced by projection and segmentation artifacts and by the limited number of available images. In addition, we analyzed 23 synthetic trees generated using R matrices computed from clinical images. A comparison of these synthetic and clinical images yielded a rms fractional error of 11%, suggesting the possibility that a more appropriate model of the ductal branching morphology may be developed. Rejection of the RBT model also suggests the existence of a relationship between ductal branching morphology and the state of mammary development and pathology. [DOI: 10.1118/1.1586453]

Key words: mammography simulation, breast ductal network, galactography, branching analysis, ramification matrices

I. INTRODUCTION

A model of the breast ductal network has been developed as a component of a 3-D computer-generated breast phantom[1] used in an approach to generate simulated mammograms. The breast phantom and mammography simulation have been proposed for analyzing the effects of breast positioning and compression during mammography, estimation of the radiation dose received during mammography,[2] development and optimization of breast imaging modalities (e.g., tomosynthesis, stereomammography, etc.), mammogram sequence registration, and the development and evaluation of computer-aided diagnosis methods. The synthetic mammograms produced using the breast phantom have been previously evaluated by texture analysis.[3] In this paper, the model of the ductal network is assessed.

The breast is a modified sweat gland, located at mid-thorax, within the superficial fascia beneath the skin.[4,5] The gland develops under genetic and hormonal influences from very early life, with a significant development in women during puberty. The adult female breast consists of 15–20 irregularly shaped lobes, i.e., subnetworks of breast ducts, converging to the nipple. The lobes are not physically separated and the branches from various lobes can overlap. Local growth of the ductal epithelial tissue is influenced by hormonal activity as well as by signaling from the surrounding stromal tissue.[6,7] The existence of ductal anastomoses, connections between the ducts from different breast lobes, has been discussed in the literature but is not uniformly accepted among researchers.[8,9] Each lobe is drained by a major duct, extending from the nipple toward the chest wall in a branching network of smaller ducts. Several major ducts join in a dilated segment beneath the nipple, known as the ampulla or lactiferous sinus. There are six to eight orifices in the nipple. The major ducts and the nipple openings are 2–4.5 mm and 0.4–0.7 mm in diameter, respectively.[10,11] Branching of the ducts toward the chest wall continues until a duct finally ends in blunt finger-like ductules formed by the acini, the basic glandular secretory units. Lobules consist of the acini surrounded by specialized connective tissue. The lobules, together with the associated terminal duct, are histologically identified as the terminal ductal lobular unit (TDLU). Hormonal influences in the adult female breast during pregnancy

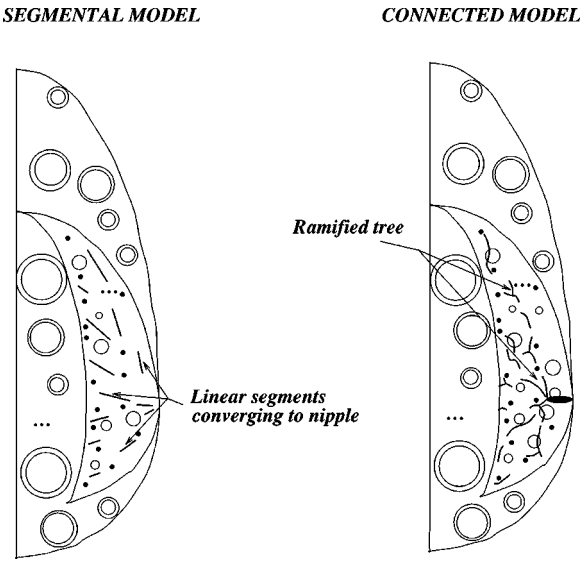

FIG. 1. Two approaches to simulate breast ducts illustrated by sections of the breast software phantom. Segmental model (left) contains short linear segments distributed within the predominantly fibroglandular tissue region, with the average direction toward the nipple. A connected model (right) consists of a computer generated ramified tree-like structure. Note that the connected tree-like structure appears in the model section as a collection of segments. Small spheres simulate TDLUs in both segmental and connected duct models.

result in the proliferation and differentiation of the TDLU's, ultimately responsible for the production of milk, which is stored in the ducts and expressed through the nipple. Involution occurs after weaning following each pregnancy. This developmental cycle can be repeated until the atrophy of ductal and lobular structures in the post-menopausal breast, unless the woman is on hormone-replacement therapy.

The ductal network is an important element of the breast anatomy since practically all breast cancers originate in the ductal (≈90%) or lobular (≈10%) epithelium, with very few arising in the connective or adipose tissue.[4] It is believed that these breast carcinomas most often begin development by spreading along the lumen of the ducts or lobules. For this reason microcalcification clusters associated with early breast cancer often follow a ductal distribution.[12] Alternatively, some breast cancers are revealed by nipple discharge with no palpable or mammographically visible lesions. Such cases are usually evaluated using galactography, a procedure for imaging the contrast-enhanced ductal network.[13–15] There has also been an increased interest in breast duct examination for the early detection of cancer using several approaches, e.g., breast lavage,[16] nipple aspirate fluid analysis,[17] or ductoscopy.[8,18] Breast ducts also contribute to the parenchymal pattern, the background texture in mammograms. It has been shown that there is a correlation between the appearance of the parenchyma and the risk of breast cancer.[19,20]

We have considered two approaches for modeling the breast ductal network, shown in Fig. 1: (1) an approximation of the ducts by short linear segments, placed randomly within the predominantly fibroglandular tissue region and oriented toward the nipple;[21,22] and (2) a tree model of the ductal network.[1] The segmental approximation is consistent with published descriptions of mammographic image elements,[23] since only short segments of the ductal network can be seen distinctly in mammograms, albeit with minimal contrast. This linear approximation roughly simulates the appearance of ducts in mammograms but was found to lack realism by neglecting connectivity, and thus will not be discussed further.

More realistic models of the ductal network can be achieved by a variety of tree modeling algorithms.[24–26] Modeling of a tree is typically approached at two levels. At the topological level, the tree is described in terms of the connections between nodes (i.e., duct branching points). At the metrical level, the lengths and spatial directions of the branches are specified. In an example of a computer-generated tree model of breast ducts, Taylor *et al.*[27] used an algorithm based upon fractal set theory, justified by the self-similarity of ductal sub-trees within the entire tree. In their work, the topological branching pattern of a perfectly balanced binary tree (each duct branches uniformly into two identical new segments) was used for all simulated trees, producing a very regular image texture. We postulated that the realism of the textural appearance would be improved by the introduction of a stochastically-generated branching pattern.

The ductal network model used in our 3-D breast phantom[1] is based upon ramification matrix analysis[26] to provide a realistic appearing ductal branching pattern. Ramification matrices (R matrices) represent parameters in a stochastic model for generating trees at the topological level. The R-matrix elements represent probabilities of different patterns of branching for the nodes at various levels of a tree. Vannimenus and Viennot[28] have observed that a large variety of botanical trees can be simulated by varying the topological parameters (branching probabilities), using the same geometric construction rules (branch widths and branching angles). This is in contrast with the frequently used computer graphics approach of modeling diverse tree forms by changing the metric rules while using a fixed topological tree. R matrices are an extension of approaches used by Horton[29] and Strahler[30] in geological studies of river networks. Woldenberg[31] listed various natural hierarchical structures that can be analyzed using a similar approach. A section of the breast phantom incorporating this connected ductal model is shown in Fig. 1(b). Note that the simulated ductal trees in the phantom section appear as a collection of segments passing through the section.

An algorithm for tree generation based upon R matrices is described in the next section. Results of an evaluation of the proposed model of the ductal network, by comparing the R matrices computed on synthetic ductal trees and on clinical galactograms, are given in Sec. III.

II. MATERIALS AND METHODS

A. Implementation of the ductal network model

The ductal network model is implemented based upon the description of branching patterns of tree-like structures given

by R matrices. The model was developed using two algorithms: one for computing R matrices from a given tree and another for generating tree topology from a given or inferred R matrix. The tree generation algorithm was used to simulate the ductal network, assuming a branching pattern of random binary trees (RBTs) that, in theory, minimally constrains the tree morphology.[26] We have analyzed clinical galactograms by computing their R matrices in order to evaluate the proposed ductal model. Evaluation results are given in Sec. III. The following is a brief description of the R-matrix computation and tree generation, and the selection of the properties of the metrical trees used for duct simulation.

1. Computation of an R matrix from a given tree

The algorithm begins by identifying the root, the internal and terminal nodes, and the branches between the nodes in a tree. Next, the nodes are labeled by their orders and biorders, as follows.

(1) All terminal nodes have order 1.
(2) An internal node, with children nodes of orders i and j, assuming binary branching, will have order $\max(i,j)$ if $i \neq j$ or $(i+1)$ if $i=j$. The labeling procedure continues until reaching the root node. The order of the root node, s, is called the Strahler number of the tree structure, and measures the topological size of a tree.[28]
(3) A parent node of order k, with two children-nodes of orders i and j, with $i \geqslant j$, has biorder (i,j).

The R matrix of a tree-like structure with Strahler number s is a lower triangular matrix of size $(s-1)\times s$, defined as[26]

$$R=[r_{k,j}=b_{k,j}/a_k, k\in(2,s), j\in(1,k)], \tag{1}$$

where a_k is equal to the number of nodes with order k $(k \geqslant 2)$. For $j<k$, $b_{k,j}$ is the number of nodes with biorder (k,j), while for $j=k$, $b_{k,j}$ is the number of nodes with biorder $(k-1,k-1)$, $(k\geqslant 2)$. Therefore, $r_{k,j}=b_{k,j}/a_k$ is the probability for a node of order k to have biorder $(k-\delta_{k,j}, j-\delta_{k,j})$, where $\delta_{k,j}$ is the Kronecker delta.

For example, the R matrix corresponding to $s=4$ has, at most, nine nonzero elements:

$$R(s=4)=\begin{bmatrix} r_{2,1} & r_{2,2} & 0 & 0 \\ r_{3,1} & r_{3,2} & r_{3,3} & 0 \\ r_{4,1} & r_{4,2} & r_{4,3} & r_{4,4} \end{bmatrix}. \tag{2}$$

2. Generation of a topological tree from a given R matrix

A given R matrix, determined either experimentally or from theoretical considerations, defines a stochastic process for the generation of binary trees. The algorithm which defines this process begins with an incomplete tree containing of only the root node. This root node is assigned an order s, corresponding to the Strahler number of the R matrix, i.e., the Strahler number that the tree will have when completed. At each iteration, a node with assigned order $k>1$, which does not yet have child nodes, is selected and assigned a pair of child nodes. These new child nodes are randomly assigned orders based on the probabilities given by the R-matrix elements $r_{k,1},\ldots,r_{k,k-1}$, $r_{k,k}$, [see Eq. (1)]. Here, $r_{k,1},\ldots,r_{k,k-1}$ are the probabilities that the child nodes will be assigned orders $(k,1),\ldots,(k,k-1)$, respectively, and $r_{k,k}$ is the probability that the assigned orders will be $(k-1, k-1)$. When there remains no childless nodes of order greater than one, the tree is complete. Once the tree is completed, the orders assigned to each node during construction agree with the orders that would be determined by the application of the algorithm in Sec. II A 1 to the completed tree.

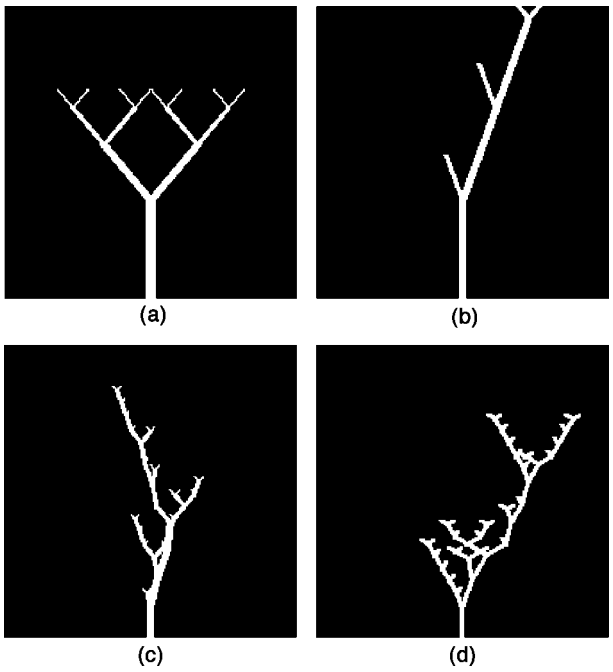

FIG. 2. Examples of computer-generated trees. (a) A perfectly balanced tree. (b) A thin fern. (c) and (d) Two random binary trees, generated using different seeds for random number generation.

As an illustration of the algorithm, a few examples of R matrices and the corresponding tree models are given in Fig. 2. Trees in Figs. 2(a) and 2(b) are a perfectly balanced tree and a thin fern, respectively, with the R matrices equal to

$$R_{\text{Perf Balance}}=\begin{bmatrix} 0 & 1 & 0 & 0 \\ 0 & 0 & 1 & 0 \\ 0 & 0 & 0 & 1 \end{bmatrix}, \quad R_{\text{Fern}}=[0.9 \;\; 0.1]. \tag{3}$$

Two random binary trees, with $s=4$ in Figs. 2(c) and 2(d) are generated with the same R matrix equal to

$$R_{\text{RBT}}=\begin{bmatrix} 0.5 & 0.5 & 0 & 0 \\ 0.5 & 0.25 & 0.25 & 0 \\ 0.5 & 0.25 & 0.125 & 0.125 \end{bmatrix}, \tag{4}$$

using two different seeds for random number generation.

3. Selection of topological and metrical tree properties

The proposed 3-D model of the breast ductal network consists of several ramified trees, each representing a ductal lobe. Each ductal lobe is modeled by an RBT. The ampulla, modeled by a short, ellipsoidal widening beneath the nipple, connects the roots of all the trees. In this work, the ampulla is modeled as 10 mm long and 4 mm in diameter. There are no published results on the statistics of branching of the breast ductal network. Thus, we selected RBTs for modeling ductal lobes, since they represent theoretically a minimum of constraints on the tree morphology.[26] The R matrix used for generation of the RBTs, given by Eq. (4), represents the asymptotic values of branching probabilities when the number of nodes in a tree increases to infinity.[26,32] Each lobe was generated using the same matrix; the variation in the appearance of the lobes is due to the stochastic nature of the tree generating process.

The number of branching levels of a tree is related to the order of the tree root and this parameter is specified at the beginning of the simulation. Real ductal trees have a relatively high number of branching levels. However, only the larger ducts are visualized by galactography. Based on an initial analysis of several galactograms, we limited the tree root order to $s=4$.

The metrical structure of each tree is generated in two steps. First, a *vertical tree* is generated in a separate rectangular coordinate system. This vertical tree is then mapped into the coordinate system of the simulated breast. The length λ and radius ρ of the individual branches decrease with the order k of the associated distal node according to

$$\lambda(k)=\lambda(s)\frac{k}{s} \quad \text{and} \quad \rho(k)=\rho(s)\frac{k}{s}, \tag{5}$$

where s is the order of the root node. Preliminary values of $\lambda(s)$ and $\rho(s)$ were selected as 1 cm and 1 mm, respectively. More accurate values of these parameters will be estimated from future analyses of a larger number of galactograms.

In producing the vertical tree, initially, a vertical branch is associated with the root node. At each node of order $k>1$, the branches leading to the child nodes are generated in a plane containing the vertical axis and rotated at an angle ϕ about the vertical axis. The angle ϕ is determined by

$$\phi=\phi_p+\Phi'+90° \tag{6}$$

where ϕ_p is the angle of rotation used at the parent node, Φ' is a random angle uniformly selected in the interval $[-15°,15°]$, and the phyllotaxy of the branching network is assumed to be such that the plane of branching rotates by approximately 90° between parent and child nodes. Within this plane, the branches to the child nodes are at angles θ_1 and θ_2 relative to the vertical axis, where

$$\theta_1=60°+\Theta', \quad \theta_2=-60°+\Theta', \tag{7}$$

when the orders of both children ducts are the same, and

$$\theta_1=(30°+\Theta'')\frac{j}{k-1}, \quad \theta_2=(-30°+\Theta'')\frac{k-j}{k-1}, \tag{8}$$

when the orders of the children ducts are j and $k\neq j$ $(k\neq 1)$. Θ' and Θ'' are randomly chosen from the intervals $[-10°,10°]$ and $[-5°,5°]$, respectively. A more accurate estimate of the angles ϕ, θ_1, and θ_2 will be possible after a future analysis of 3D images of the breast ductal network.

The mapping of a vertical tree into the geometry of the breast phantom is determined by (i) the position of the ampulla, serving as an anterior endpoint and connecting root nodes of all simulated lobes, (ii) the chosen posterior endpoint on the intersection of the anterior and posterior ellipsoidal borders of the phantom fibroglandular region (see Fig. 3 in Ref. 1), and (iii) a curved path, an arch, connecting the two endpoints defined by (i) and (ii). This arch, modeling the curvature of the simulated lobe, is defined by a user-supplied angle between the root of the lobe and the straight line connecting the two endpoints. In this work, a lobe curvature angle of 20° was used. In the simulated lobe, each branch is generated with position and direction relative to the arch of the lobe [defined in (iii)], equal to the position and direction of the corresponding branch in the vertical tree relative to the tree's vertical axis. The posterior end points for each tree are selected, assuming an approximately equal angular distance between the lobes around the nipple–chest wall line, as suggested by an ultrasound analysis of breast ducts.[33]

In addition to the ramified trees, our 3-D breast phantom includes models of the TDLUs. Each TDLU is simulated by a sphere of 1–2 mm diameter, according to descriptions in the literature.[4,23] Examples of some simulated ducts are shown in Fig. 3. Projections of individual ductal lobes are shown in Figs. 3(a) and 3(b), and a projection of five simulated lobes is given in Fig. 3(c). For clarity, all other simulated medium scale anatomic structures[1] have been suppressed in these images. Several views of the same five simulated lobes, generated from a virtual reality representation, were shown in Fig. 6 of Ref. 1. The virtual reality representation was generated using the VRML modeling language[34] by transforming each voxel of the 3-D model of the ductal network into a cube within the virtual reality space. This virtual reality representation of the five simulated lobes is available via EPAPS.[35]

B. Evaluation of the ductal network model

We evaluated the breast ductal network model by comparing simulated trees with real ducts from galactogram images. Ducts are barely seen in conventional mammograms. On the other hand, galactograms, x-ray images of the breast with contrast enhanced ducts, allow the visualization and analysis of the ductal network. We have retrospectively analyzed clinical galactograms from 15 patients imaged at the Thomas Jefferson University Breast Imaging Center (Philadelphia, PA) during a period of six and a half years (June 1994–January 2001). The total number of patients who had undergone galactography during this period was 41. Galactograms from 17 patients were unavailable because they had been returned to the patients or the primary health care institutions, and galactograms from another nine patients were not used because of obstruction or poor image quality. The mean

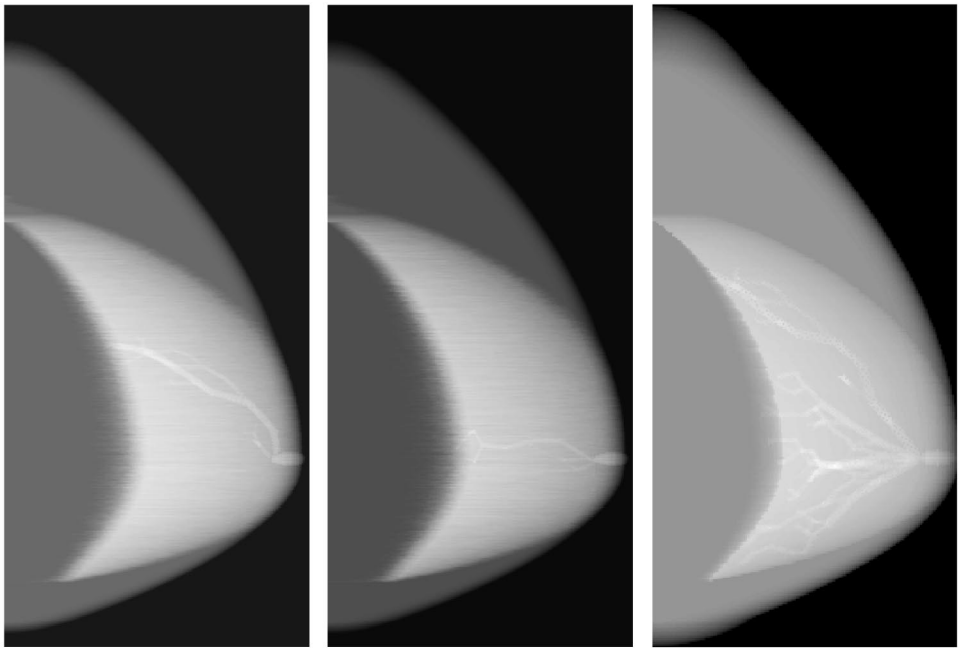

FIG. 3. Examples of computer-generated duct lobes. (a) and (b) Two synthetic mammograms, each with a single simulated duct lobe. (c) A simulated mammogram with five duct lobes. (In these simulated images, other simulated anatomical structures, e.g., Cooper's ligaments and adipose compartments, have been suppressed.)

age of the 15 patients whose cases were analyzed, was 49.2 years (range, 29–75 years). Of these 15 patients, eight (mean age, 44.2 years; range, 29–74 years) had no reported galactographic findings and seven (mean age, 54.8 years; range, 43–75 years) had findings of ductal ectasia, cysts, or papilloma. There were no reported findings of malignancy from the analyzed cases.

Here 25 galactograms from the 15 patients were analyzed: nine mediolateral or mediolateral oblique views (hereafter referred to in combination as ML/MLO) and 16 craniocaudal views (CC). Out of 25 galactograms, there were (i) 3 MLO views (2 right and 1 left) and 6 ML views (3 right and 3 left), and (ii) 16 CC views, 9 of the right breast and 7 of the left. One of the ML views was magnified. In one case, two lobes of the same breast were imaged. (A comprehensive list of patient data, showing their ages, the views available for this study, the symptoms, and the radiologists' diagnoses, is tabulated in our previous publication.[36])

The evaluation of the ductal network model was performed using the following steps. First, the branching structures in clinical and synthetic images were identified and segmented, and the corresponding R matrices were computed. Second, the R-matrix elements were averaged over all the nodes in the clinical and synthetic ductal trees, and the averaged matrices were statistically compared. The node averaging is discussed in more detail in Section II B 2 and the Appendix.

The resultant ductal trees were also analyzed in terms of their bifurcation ratios, providing an alternative means of describing ramified patterns. These were originally introduced for analyzing river topologies and the tree structure of fluvial basins.[29,30] A bifurcation ratio is defined as the ratio between the number of tree segments of two consecutive orders. A segment of order k is defined as the longest sequence of consecutive tree branches starting on a node of order k and ending at a node of order $m>k$. Thus,[28]

$$\beta_k = \Sigma_k / \Sigma_{k+1}, \tag{9}$$

where Σ_k and Σ_{k+1} are the numbers of segments of order k and $(k+1)$, respectively. The bifurcation ratios corresponding to an RBT are equal to $\beta_1=\beta_2=\beta_3=4$.[28]

The algorithm for computing R matrices, adopted from Viennot *et al.*,[26] was described in Sec. II A 1, while here we focus on the practical problems of tracing the ductal network from clinical images and a statistical comparison of the computed parameters.

1. Tracing the ductal network from galactograms

We traced the network of larger ducts from the clinical galactograms in order to reconstruct their topological structure. A significant difficulty in this approach, due to the projective nature of galactograms, is distinguishing the points where ducts branch from the points where they overlap. We adopted an *ad hoc* reasoning based on the assumption that points where ducts overlap look brighter than the points of duct branching, due to the superposition of the x-ray attenuation of two ducts on top of each other, as illustrated in Fig. 4. This approach is, however, still sensitive to (i) the orientation of the plane in which the duct branches with respect to the film plane, (ii) the effects of overlapping of more than two ducts at the same point, and (iii) nonuniform filling of all ducts with contrast agent.

An identification of the branching pattern was done manually by placing a galactogram under a semitransparent tracing paper on a light box. The procedure consists of three basic operations: (1) marking the points where large ducts branch or overlap, (2) distinguishing between branching and

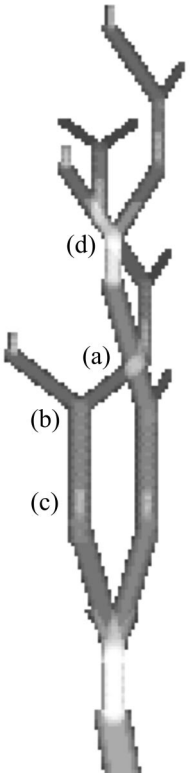

FIG. 4. An illustration of the identification of branching structures on a part of a synthetic galactogram. The point where ducts overlap (a) is brighter than the point of branching (b), except when the orientation of the plane in which the duct branches significantly differs from the film plane (c), or when there are many ducts overlapping at the same point (d).

overlap based on the intensity of the marked points, and (3) connecting the marked points to reconstruct the large ducts. Figure 5 shows an example of an original galactogram and the corresponding network of manually traced larger ducts.

Figure 5 illustrates the computation of the R matrix from a manually-traced clinical ductal tree, using the procedure described in Sec. II A 1. Figure 5(b) shows the manually-traced branches of the segmented ductal network from a clinical galactogram shown in Fig. 5(a). Different symbols represent the nodes of different order (circle=order 2, triangle=order 3, and square=order 4). The corresponding R matrix is equal to

$$R=\begin{bmatrix} r_{2,1} & r_{2,2} & \cdot & \cdot \\ r_{3,1} & r_{3,2} & r_{3,3} & \cdot \\ r_{4,1} & r_{4,2} & r_{4,3} & r_{4,4} \end{bmatrix} = \begin{bmatrix} 0.50 & 0.50 & \cdot & \cdot \\ 0.31 & 0.50 & 0.19 & \cdot \\ 0.40 & 0.20 & 0.20 & 0.20 \end{bmatrix}. \quad (10)$$

To illustrate the computation of Eq. (10), there is a total of 30 nodes with order 2 (labeled by circles). Of these, 15 nodes have biorder (2,1), i.e., their child nodes are of orders 2 and 1, corresponding to the probability of $r_{2,1}=15/30=0.5$. The remaining 15 nodes of order 2 have biorder (1,1), i.e., they bifurcate into pairs of branches both ending in a terminal node, corresponding to the probability of $r_{2,2}=15/30=0.5$. In a similar manner all the elements of the R matrix shown in Eq. (10) were computed from the galactogram shown in Fig. 5(a). In this paper we computed R matrices with nine elements and Strahler number $s=4$, corresponding to a root branch with label 4. The bifurcation ratios corresponding to the same ductal tree are equal to $\beta_1=3.47$, $\beta_2=5.00$, $\beta_3=3.00$. To illustrate a computation of the bifurcation ratios, segments of order 3 and order 4 are denoted in Fig. 5(b). There are three segments of order 3: (i) **a–a′**, (ii) **a–a″**, and (iii) **b–b′**. The only segment of order 4, **a–c**, connects all the nodes of order 4. Using Eq. (9), the value of the bifurcation ratio β_3 is equal to $\beta_3=\Sigma_3/\Sigma_4=3/1=3$.

We have also analyzed synthetic galactograms generated by the projection of 3-D RBT models of individual ductal lobes. The R matrices were computed from the projections of simulated vertical ductal trees, rather than using the theoretical R matrix corresponding to the RBT. By working with clinical and synthetic trees in a comparable manner, systematic errors were minimized. Twenty-five synthetic galactograms have been analyzed. Manual tracing was successful in 23 images; the projection of the synthetic trees in two images contained too many ambiguous points of branching or overlap, which prevented the successful identification of the branching trees.

2. Statistical comparison of clinical and synthetic R matrices

In this paper we have evaluated synthetic ductal networks by comparing R matrices and bifurcation ratios computed from clinical and synthetic images. We will describe in detail the comparison of the R-matrix elements; bifurcation ratios have been evaluated using a similar approach.

Elements of the R matrices computed from manually-traced ductal trees represent estimates of the probabilities of branching at different levels of a tree. Each matrix element is equal to the ratio between the number of nodes with a given biorder (see Sec. II A 1) and the total number of nodes of the corresponding order. With this in mind, there are two ways of averaging the R-matrix element values for a given set of trees[32] (see the Appendix). An estimate of the R-matrix appropriate for modeling a population of trees is obtained using the *node-averages*, $P_{k,j}$. Nodes of the same order from all the trees in the analyzed set are grouped together, and the node-averaged matrix element $P_{k,j}$ is the fraction of nodes with a given biorder [see Eq. (A1)]. The *tree-average*, $Q_{k,j}$, is the average of R matrices computed for individual trees [see Eq. (A2)]. This gives an estimate of the R matrix corresponding to an individual tree from the analyzed set. Node averaging, relative to tree averaging, generally gives more weight to nodes in larger trees. As discussed in the Appendix, node averaging provides a less biased estimate of the R matrix that generated the trees.

We have been analyzing the branching morphology of the ductal networks traced from the clinical and synthetic images, which, for the purpose of comparison, can be considered two families of trees. Thus, an appropriate approach is to use the node averages of R matrices. In our previously

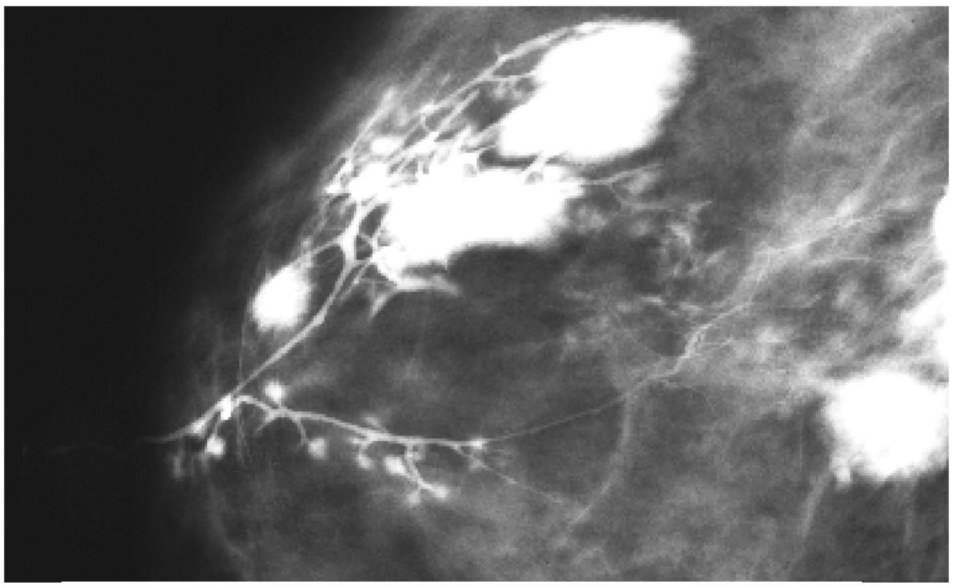

(a)

(b)

FIG. 5. An example of tracing the ductal tree branching pattern from a clinical galactogram (right CC view). (a) A detail of the galactogram with a contrast-enhanced ductal network. (Large bright regions are due to extravasation, which did not affect the segmentation of the ductal tree.) (b) The manually traced tree of larger ducts from the galactogram shown in (a), with the tree nodes of different order labeled by symbols (circle=order 2, triangle=order 3, and square=order 4). Also, shown are three segments of order 3: (**a**,**a**′), (**a**,**a**″), and (**b**,**b**′), and the segment of order 4: (**a**,**c**).

published work on the classification of galactograms using R matrices,[36] the R matrices corresponding to each analyzed ductal tree were compared with the tree averages computed from two analyzed classes of galactograms, as the expected values of an individual tree.

The uncertainty in estimates of the R-matrix elements and the bifurcation ratios were estimated using counting statistics, e.g., the number of nodes $b_{k,j}$ with specified biorder was taken as having an uncertainty of $s_{b_{k,j}} \approx \sqrt{b_{k,j}}$. The uncertainties were treated as uncorrelated, which is acceptable given the limited number of cases. Thus, the standard errors of the node-averaged R-matrix elements, $s_{P_{k,j}}$, have been estimated by

$$s_{P_{k,j}} = s\left(P_{k,j} = \frac{\Sigma_T b_{k,j}^T}{\Sigma_T a_k^T} = \frac{B_{k,j}}{A_k} \right) = \sqrt{\left(\frac{s_{B_{k,j}} A_k}{A_k^2} \right)^2 + \left(\frac{B_{k,j} s_{A_k}}{A_k^2} \right)^2} \approx \sqrt{\frac{B_{k,j}}{A_k^2} + \frac{B_{k,j}^2}{A_k^3}}. \tag{11}$$

A more accurate estimate of the standard error in node-averaged R-matrix elements requires a bootstrap approach.

Node-averaged values of the R matrices were compared (i) by computing differences between individual matrix elements for the clinical and synthetic images, and (ii) by com-

TABLE I. The average number of traced ducts per tree, N_{branch}, and the average number of nodes (i.e., the branching points) per tree, N_{node}, for the analyzed clinical and synthetic ductal trees. a_k correspond to the average number of nodes of order k.

	Clinical, traced (All)	(ML/MLO only)	(CC only)	Synthetic, traced
N_{branch}	61.5±5.1	56.8±6.5	64.1±7.1	79.4±7.9
N_{node}	30.2±2.6	27.9±3.3	31.5±3.6	39.2±3.9
a_2	16.7±1.5	14.8±1.8	17.8±2.1	19.7±1.9
a_3	8.6±0.9	8.4±1.3	8.6±1.2	11.0±1.5
a_4	5.0±0.6	4.7±0.7	5.12±0.8	8.4±1.3

puting a root-mean-square (rms) fractional error of simulation for the whole matrix. The rms fractional error is given by

$$D=\sqrt{\sum_{k=2}^{s}\sum_{j=1}^{k}\left[\frac{P_{k,j}^{\text{sim}}-P_{k,j}^{\text{clin}}}{P_{k,j}^{\text{clin}}}\right]^2 \Big/ N_{\text{el}}}, \tag{12}$$

where $P_{k,j}^{\text{sim}}$ and $P_{k,j}^{\text{clin}}$ are the R-matrix elements averaged over all simulated and all clinical trees, respectively. N_{el} is the number of nonzero R-matrix elements. $N_{\text{el}}\leqslant 9$ for $s=4$, from Eq. (2).

III. RESULTS

The branching morphology of the breast ductal networks has been traced manually from 25 clinical galactograms (9 ML/MLO and 16 CC views) and 23 projections of simulated RBTs. The average number of traced ducts per tree and the average numbers of nodes (i.e., the branching points) per tree are given in Table I. Results of comparing clinical trees and synthetic random binary trees in terms of R matrices and bifurcation ratios are given below.

A. Comparison of the R-matrix elements

Figure 6 compares the R-matrix elements used to generate the simulated trees (theoretical) with the node averages of the simulated trees (computed) and the node averages resulting from manually tracing the same set of simulated trees (traced). Theoretical matrix elements are computed in the limit when the number of tree nodes increases to infinity.[26,32] By using manual tracings of projections of the simulated trees, the effects of projection and segmentation artifacts were tested. In case of perfect segmentation of all branches without ambiguities, the traced and computed values of the R matrices would be the same. The rms fractional error between the theoretical and simulated RBTs was 6.3%. The rms fractional error between the computed values and the values recovered by manually tracing the simulated projections was 1.8%.

Values of the R-matrix elements, node averaged over manually traced clinical ductal trees and over manually traced synthetic RBTs, are given in Table II and shown in Fig. 7. Table II also gives the expected uncertainties in the node-averaged matrix element values, estimated as described in Sec. II B 2. Variations in R matrices of individual trees

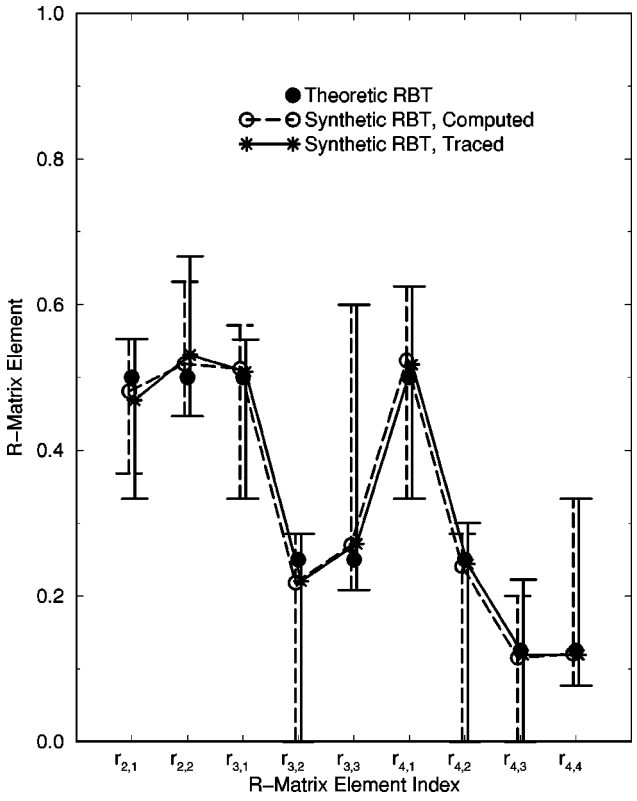

FIG. 6. A comparison of the theoretical R-matrix elements for random binary trees and the matrix elements computed for 23 simulated and manually traced simulated random binary trees. The theoretical values have been computed for the limit when the number of tree nodes increases to infinity. For the synthetic random binary trees, symbols correspond to the node-averaged matrix element values and the error bars correspond to 25–75-percentile ranges.

over the population of all clinical and synthetic trees are illustrated in Fig. 7 by the 25–75-percentile ranges.

The differences between the node-averaged R-matrix elements, corresponding to the manually traced clinical and simulated trees are

$$\Delta R=R^{\text{sim}}-R^{\text{clin}} =\begin{bmatrix} 0.085 & -0.085 & \times & \times \\ 0.176 & -0.088 & -0.088 & \times \\ 0.228 & -0.039 & -0.107 & -0.082 \end{bmatrix}, \tag{13}$$

corresponding to a rms fractional error of 41%.

B. Comparison of the bifurcation ratios

The bifurcation ratios computed from the clinical galactograms and the projections of simulated RBTs are given in Table III. The differences between the node-averaged bifurcation ratios, corresponding to the manually traced clinical and simulated trees are

$$\begin{aligned} \Delta(\beta_1)&=\beta_1^{\text{sim}}-\beta_1^{\text{clin}}=0.75,\\ \Delta(\beta_2)&=\beta_2^{\text{sim}}-\beta_2^{\text{clin}}=0.72,\\ \Delta(\beta_3)&=\beta_3^{\text{sim}}-\beta_3^{\text{clin}}=-0.12, \end{aligned} \tag{14}$$

TABLE II. Theoretical values of the R-matrix elements for random binary trees and node averages of the matrix elements computed for 23 simulated, 23 manually traced simulated, and 25 manually traced clinical ductal trees. (See Figs. 6 and 7.)

	Theoretic	Synthetic	Synthetic, traced	Clinical, traced (All)	(ML/MLO only)	(CC only)
$r_{2,1}$	0.500	0.481±0.040	0.469±0.039	0.384±0.036	0.361±0.061	0.394±0.044
$r_{2,2}$	0.500	0.519±0.042	0.531±0.042	0.616±0.049	0.639±0.089	0.606±0.058
$r_{3,1}$	0.500	0.512±0.055	0.508±0.055	0.332±0.045	0.355±0.080	0.319±0.055
$r_{3,2}$	0.250	0.218±0.032	0.220±0.032	0.308±0.043	0.289±0.070	0.319±0.055
$r_{3,3}$	0.250	0.270±0.037	0.272±0.037	0.360±0.047	0.355±0.078	0.362±0.060
$r_{4,1}$	0.500	0.524±0.065	0.518±0.064	0.290±0.055	0.357±0.107	0.256±0.063
$r_{4,2}$	0.250	0.241±0.040	0.244±0.040	0.282±0.054	0.214±0.079	0.317±0.071
$r_{4,3}$	0.125	0.115±0.026	0.119±0.026	0.226±0.047	0.214±0.079	0.232±0.059
$r_{4,4}$	0.125	0.120±0.026	0.119±0.026	0.202±0.044	0.214±0.079	0.195±0.053

corresponding to a rms fractional error of 15%.

IV. DISCUSSION

We have simulated the breast ductal network assuming that the branching structure can be modeled by RBTs, which in theory minimally constrain the tree morphology. We evaluated this assumption by comparing the node-averaged values of R-matrix elements estimated from manually-traced clinical galactograms and the projections of simulated RBTs (see Fig. 7). The differences between such estimated R-matrix elements corresponding to our sets of clinical and simulated trees are given by Eq. (13). These differences are influenced by the projective nature of galactography, the manual duct-tracing procedure, and the limited number of available clinical images.

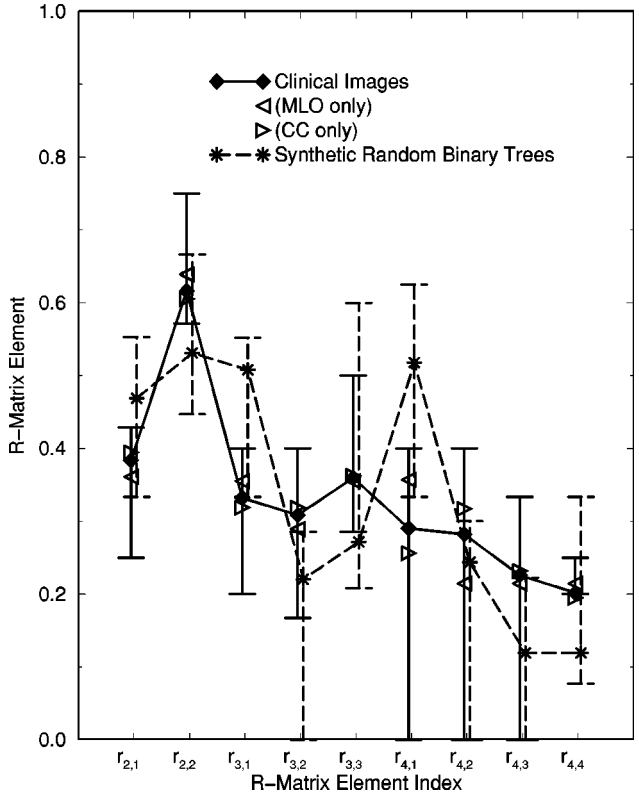

FIG. 7. A comparison of the R-matrix elements computed for 25 manually traced clinical ductal trees and for 23 manually traced synthetic random binary trees. Symbols correspond to the node-averaged matrix element values and the error bars correspond to 25–75-percentile ranges. For the clinical trees, the node averages computed for all the trees are shown (diamonds), as well as the ML/MLO views (left triangles), and CC views (right triangles).

The difference in the matrix elements estimated from simulated ductal trees and the matrix elements estimated from clinical galactograms is approximately three times their standard error (Table II). This suggests that it may be possible to develop a more appropriate model of the breast ductal network than the random binary tree. As a first step, we generated an additional set of synthetic trees using, as the input to the simulation, the node-averaged R-matrix elements corresponding to the clinical images. Note that due to the probabilistic nature of R matrices, simulation using an R matrix of a given tree will produce a variety of synthetic trees, with statistical properties similar but not identical to those of the original tree.

To match the number of clinical cases, we generated 9 synthetic trees using the node-averaged matrices computed from the clinical ML/MLO galactographic views and 16 trees using the matrices computed from clinical CC views. The R-matrix elements used for generating the synthetic trees are given in the two rightmost columns of Table II. These synthetic images were manually segmented in the same manner as the previously analyzed clinical and random binary trees (Sec. II B 1). Out of 25 simulated vertical clinical trees, we successfully traced the ductal morphology from 23 images (9 ML/MLO) and 14 CC views). The average number of branches in these 23 simulated clinical trees was 60.3±7.6. The average number of nodes in the simulated clinical images was 29.7±3.8 ($a_2=16.2\pm2.0$, $a_3=8.2\pm0.9$, and $a_4=5.3\pm1.1$, see Table I). Figure 8 shows the node averages of the R-matrix elements computed for manually traced simulated clinical trees, compared to the node-averages for the original clinical trees. The rms fractional error between the original and such simulated clinical trees is equal to 11%. A similar analysis of the bifurcation ratios gives the rms fractional error between the original and simulated clinical trees of 3.9%. The values of the fractional rms error obtained using the simulated clinical ductal trees are lower than when synthetic RBTs were used. However, an analysis of additional clinical images is necessary before we

TABLE III. Theoretical values of the bifurcation ratios (β) for random binary trees and node averages of the β values computed for 23 simulated, 23 manually traced simulated, and 25 manually traced clinical ductal trees.

	Theoretic	Synthetic	Synthetic, traced	Clinical, traced (All)	(ML/MLO only)	(CC only)
β_1	4.00	3.89±0.28	3.83±0.28	3.09±0.22	3.13±0.40	3.06±0.27
β_2	4.00	3.48±0.48	3.49±0.48	3.24±0.42	3.07±0.68	3.33±0.53
β_3	4.00	2.96±0.36	3.00±0.36	3.12±0.35	3.00±0.58	3.19±0.45

would deem it appropriate to adopt a tree model other than RBTs.

In order to further improve the model of the ductal network, we plan a future analysis of a larger number of clinical images. The reported results are potentially biased by the manual segmentation approach and the long duration of case accrual. We believe, however, that the manual segmentation was sufficiently robust as to not affect our results. In prior work, we have evaluated the effect of tree pruning[36] and did not find that the resultant R-matrices were significantly altered. Such concerns, however, have led us to consider other approaches. A three-dimensional analysis of the ductal networks (e.g., contrast-enhanced MRI or CT) is desirable in order to reduce the effects of the projective nature of galactograms. Artifacts due to the manual segmentation of the ducts can be reduced by developing an automated tracing algorithm for 3-D galactograms (similar to the reported automated methods for tracing vascular, bronchial, hepatic, or biliary networks). Another approach would be to analyze ductal casts from cadaveric breasts.

Rejection of the random binary tree model, a minimally constrained model, additionally suggests that ductal branching does not occur by chance alone; there might be some information about the developmental or pathological state of the breast encoded in the ductal branching pattern. This assumption is supported by our preliminary results in classifying images with and without galactographic findings of cysts, ductal ectasia, and papilloma, using the values of R-matrix elements.[36] The relationship between the ductal morphology and breast lesions has been known pathologically but has not been previously quantitatively described from macroscopic radiological images. We would also like to extend this approach to analyses of the branching pattern in murine mammary ducts under various controlled hormonal or carcinogenic influences, following the work of Atwood *et al.*[6]

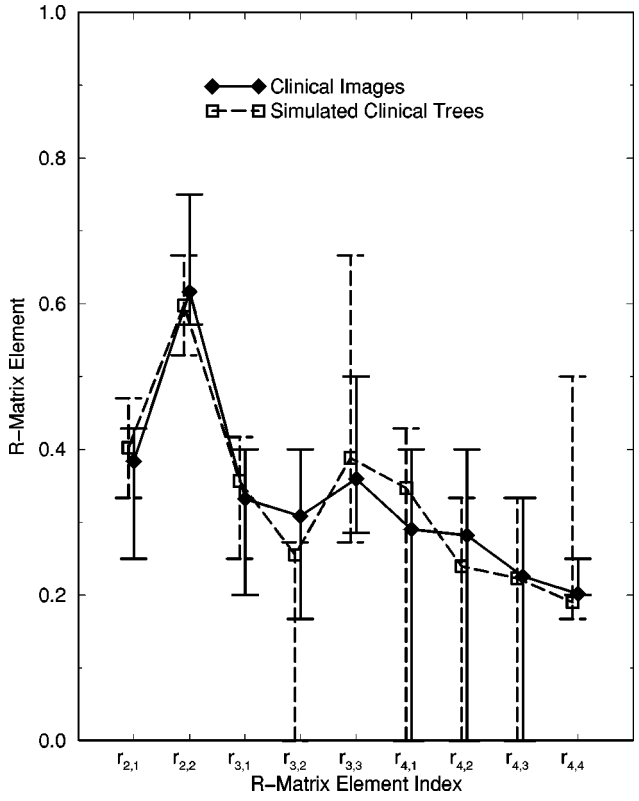

FIG. 8. A comparison of the R-matrix elements computed for 25 manually traced clinical ductal trees and for 23 manually traced simulated clinical trees (see Sec. IV). Symbols correspond to the node-averaged matrix element values and the error bars correspond to 25–75-percentile ranges.

V. CONCLUSIONS

An attempt to simulate the breast ductal network branching morphology is reported. The ductal network is modeled by a collection of binary trees, each representing a ductal lobe. The branching morphology is described using ramification matrices, whose elements—equal to the probabilities of different patterns of branching for the nodes at various levels of a ramified tree—represent parameters in a stochastic model for generating the ductal tree topology. Lacking sufficient knowledge about the statistics of ductal branching, preliminarily, we approximated each lobe by a random binary tree, in theory, the least constrained model of topology. A statistical comparison between manually traced ductal trees from a small number of clinical galactograms and synthetic random binary trees indicates a certain degree of disagreement, suggesting the possibility of developing a more appropriate model of the ductal network topology in the future. This, in turn, suggests that the ductal branching morphology might be indicative of the state of development or health of the breast. Furthermore, ramification matrices may be an efficacious methodology for quantification of this morphology.

ACKNOWLEDGMENTS

This work was supported in part by National Science Foundation Grant No. IRI-9504363 and by U.S. Army Breast Cancer Research Program Grants No. DAMD 17-96-1-6128 and No. DAMD 17-98-1-8169.

APPENDIX: TREE AND NODE AVERAGING OF R-MATRIX ELEMENTS

The stochastic algorithm for generating topological trees used in this paper can be viewed as randomly selecting a binary tree from the family of all binary trees with a predetermined Strahler number (here equal to 4). The probability that the algorithm will generate or select a given tree is simply the product of the R-matrix elements associated with all of the nodes of order greater than one in the tree.

Given a set of trees, which are presumed to be samples from a random process that can be modeled in this manner, it is reasonable to attempt to estimate the appropriate values of the corresponding R matrix. Here, one must use caution. Following Penaud,[32] from a set of trees one can estimate the R-matrix values by counting all relevant nodes in all trees, so that

$$P_{k,i}=\frac{\Sigma_T b_{k,i}^T}{\Sigma_T a_k^T}, \tag{A1}$$

where T is an index over the n trees in the set and a_k^T and $b_{k,i}^T$ are the counts of the numbers of nodes with appropriate order and biorder, respectively. This "node average" is referred to by Penaud as the "*matrice de ramification d'une famille.*" Alternatively, one can compute ramification matrices for each tree, then average over the set of trees, obtaining the "tree average,"

$$Q_{k,i}=\frac{1}{n}\sum_T \frac{b_{k,i}^T}{a_k^T}, \tag{A2}$$

which Penaud refers to as the "*matrice de ramification d'un arbre aléatoire d'une famille.*"

The node average and tree average are not necessarily equal, as illustrated by Penaud with a simple example of the set of six trees with a total of four internal nodes and Strahler number three. Viennot *et al.*,[26] in introducing the algorithm that we have used, determined experimentally that the ramification matrix calculated from a given tree produced by this stochastic process is "close to the given matrix R, especially for the first rows (corresponding to the small orders)....."

While a full analysis of this effect is beyond this paper, a brief analysis of the $r_{4,4}$ element is illustrative. The element $r_{4,4}$ represents the probability that a given branch of the "trunk" of a tree (i.e., the tree segment of the order 4) terminates the trunk by having two nodes of lower order as descendants. If a given R matrix is used to stochastically generate random trees, and then a set of n trees so generated is used to estimate the ramification matrix,

$$\langle P_{k,i}\rangle_n=\sum_{m_1}\cdots\sum_{m_n}(q^{m_1-1}p)\cdots(q^{m_n-1}p)\frac{n}{m_1+\cdots+m_n}, \tag{A3}$$

where $p=r_{4,4}$, $q=1-p$, and m_i is the number of nodes of order 4 in the ith tree, i.e., $m_i=a_4^T$ with $T=i$ indexing the ith tree. This can be written as

$$\langle P_{k,i}\rangle_n=np^n h(q), \tag{A4}$$

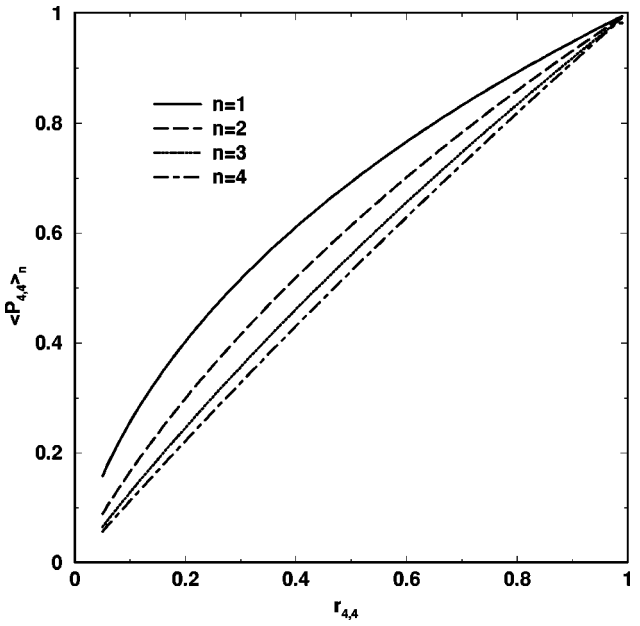

FIG. 9. An illustration of tree averaging and node averaging of the R-matrix elements (see the Appendix). The abscissa shows the value of $r_{4,4}$ used in the stochastic model for generating random trees. The ordinate shows the value of the node average, $\langle P_{4,4}\rangle_n$, which would be expected from averaging all nodes in n trees randomly generated by this model. For $n=1$, the node average and the tree average are the same when computed over a single tree, $\langle P_{4,4}\rangle_1=\langle Q_{4,4}\rangle$. The bias in the estimate of the parameters of the stochastic model for generating the random trees, $(\langle P_{4,4}\rangle_n-r_{4,4})$, quickly decreases as the number of trees increases.

where

$$h(x)=\sum_{m_1}\cdots\sum_{m_n}\frac{1}{m_1+\cdots+m_n}x^{m_1+\cdots+m_n-n} \tag{A5}$$

can be seen to satisfy the differential equation

$$\frac{d}{dx}[x^n h(x)]=\frac{x^{n-1}}{(1-x)^n}, \tag{A6}$$

and the condition that $h(0)=1/n$. Thus

$$x^n h(x)=\frac{1}{n-1}\frac{x^{n-1}}{(1-x)^{n-1}}-\frac{1}{n-2}\frac{x^{n-2}}{(1-x)^{n-2}}+\cdots$$
$$+(-1)^n\frac{x}{1-x}+(-1)^n\ln(1-x), \tag{A7}$$

where the constant of integration must be zero in order for $h(0)$ to be finite. Note that for $n=1$, corresponding to tree averages, this formula must be interpreted as

$$xh(x)=-\ln(1-x), \tag{A8}$$

with no other terms in the sum, as otherwise the term with coefficient $1/(n-1)$ would render the equation nonsensical.

The nature of this effect is illustrated in Fig. 9. The abscissa shows the value of $r_{4,4}$ used in the stochastic model. The ordinate shows the value $\langle P_{4,4}\rangle_n$, which would be expected from averaging all nodes in n trees randomly generated by this model. For $n=1$, $\langle P_{4,4}\rangle_1=\langle Q_{4,4}\rangle$. Thus "tree averages" (i.e., taking the average of the ramification matri-

ces calculated for each tree and then averaging over the set of trees) introduce a bias in the estimate of the parameters of the stochastic model. The other elements of the fourth row, $r_{4,1}$, $r_{4,2}$ and $r_{4,3}$, would be also be biased, as any estimate of the row must sum to unity. The bias quickly decreases as the number of trees increases. This also explains the observation of Viennot *et al.* that the matrix elements calculated from individual trees agree with those of the R matrix used to generate those trees for low-order elements, as each tree essentially contains multiple subtrees of a lower Strahler number.[26]

[a]Electronic mail: maidment@rad.upenn.edu

[1] P. R. Bakic, M. Albert, D. Brzakovic, and A. D. A. Maidment, ''Mammogram synthesis using 3D simulation. I. Breast tissue model and image acquisition simulation,'' Med. Phys. **29**, 2131–2139 (2002).
[2] R. A. Hunt, D. R. Dance, P. R. Bakic, A. D. A. Maidment, M. Sandborg, and G. Alm Carlsson, ''Monte Carlo simulation of x-ray mammography using a realistic voxel phantom,'' Proceedings of the UK Radiology Congress, June 2003, Birmingham, UK.
[3] P. R. Bakic, M. Albert, D. Brzakovic, and A. D. A. Maidment, ''Mammogram synthesis using 3D simulation. II. Evaluation of synthetic mammogram texture,'' Med. Phys. **29**, 2140–2151 (2002).
[4] D. B. Kopans, *Breast Imaging*, 2nd ed. (Lippincott-Raven, Philadelphia, 1998).
[5] F. A. Tavassoli, *Pathology of the Breast*, 2nd ed. (Appleton & Lange, Stamford, 1999).
[6] C. S. Atwood, R. C. Hovey, J. P. Glover, G. Chepko, E. Ginsburg, W. G. Robinson, Jr., and B. K. Vonderhaar, ''Progesterone induces side-branching of the ductal epithelium in the mammary glands of peripubertal mice,'' J. Endocrinol. **167**, 39–52 (2000).
[7] V. M. Weaver, O. W. Petersen, F. Wang, C. A. Larabell, P. Briand, C. Damsky, and M. J. Bissell, ''Reversion of the malignant phenotype of human breast cells in three-dimensional culture and in vivo by integrin blocking antibodies,'' J. Cell Biol. **137**, 231–245 (1997).
[8] S. M. Love and S. H. Barsky, ''Breast duct endoscopy to study stages of cancerous breast disease,'' Lancet **348**, 997–999 (1996).
[9] T. Ohtake, I. Kimijima, T. Fikishima, M. Yasuda, K. Sekikawa, S. Takenoshita, and R. Abe, ''Computer-assisted complete three-dimensional reconstruction of the mammary ductal/lobular systems: implications of ductal anastomoses for breast conserving surgery,'' Cancer **91**, 2263–2272 (2001).
[10] K. I. Bland and E. M. Copeland III, in *The Breast: Comprehensive Management of Benign and Malignant Diseases*, 2nd ed. (Saunders, Philadelphia, 1998).
[11] R. L. Egan, *Breast Imaging: Diagnosis and Morphology of Breast Diseases* (Saunders, Philadelphia, 1988).
[12] M. Lanyi, *Diagnosis and Differential Diagnosis of Breast Calcifications* (Springer-Verlag, Berlin, 1988).
[13] A. Gregl, *Color Atlas of Galactography: Clinical and Radiological Symptomatology and Therapy of the Secreting Breast* (F. K. Schautter-Verlag, Stuttgart, 1980).
[14] L. Tabar, P. B. Dean, and Z. Pentek, ''Galactography: the diagnostic procedure of choice for nipple discharge,'' Radiology **149**, 31–38 (1983).
[15] G. Cardenosa, C. Doudna, and G. W. Eklund, ''Ductography of the breast: technique and findings,'' Am. J. Radiol. **162**, 1081–1087 (1994).
[16] W. C. Dooley *et al.*, ''Ductal lavage for detection of cellular atypia in women at high risk for breast cancer,'' J. Natl. Cancer Inst. **93**, 1624–1632 (2001).
[17] E. R. Sauter, H. Ehya, J. Babb, E. Diamandis, M. Daly, A. J. P. Klein-Szanto, J. Hoffman, J. Malick, and P. F. Engstrom, ''Biologic markers of risk in nipple aspirate fluid are associated with residual cancer and tumor size,'' Br. J. Cancer **81**, 1222–1227 (1999).
[18] D. Yamamoto, T. Shoje, H. Kawanishi, H. Nakagawa, H. Haijima, H. Gondo, and K. Tanaka, ''A utility of ductography and fiberoptic ductoscopy for patients with nipple discharge,'' Breast Cancer Res. Treat. **70**, 103–108 (2001).
[19] J. N. Wolfe, ''Risk for breast cancer development determined by mammographic parenchymal patterns,'' Cancer **37**, 2486–2492 (1976).
[20] J. W. Byng, M. J. Yaffe, R. A. Jong, R. S. Shumak, G. A. Lockwood, D. L. Trichler, and N. F. Boyd, ''Analysis of mammographic density and breast cancer risk from digitized mammograms,'' Radiographics **18**, 1587–1598 (1998).
[21] P. Bakic, D. Brzakovic, P. Brzakovic, and Z. Zhu, ''An approach to using a generalized breast model to segment digital mammograms,'' Proceedings of the 11th IEEE Symposium on Computer-Based Medical Systems, Lubbock, TX, 1998, pp. 84–89.
[22] P. Bakic, D. Brzakovic, and Z. Zhu, ''Anatomic segmentation of mammograms via breast model,'' in *Digital Mammography Nijmegen 1998*, Proceedings of the 4th International Workshop on Digital Mammography, Nijmegen, The Netherlands, June 1998, edited by N. Karssemeijer, M. Thijssen, J. Hendriks, and L. van Erning (Kluwer Academic, Dordrecht, 1998), pp. 291–294.
[23] I. T. Gram, E. Funkhouser, and L. Tabar, ''The Tabar classification of mammographic parenchymal patterns,'' Eur. J. Radiol. **24**, 131–136 (1997).
[24] P. Prusinkiewicz, A. Lindenmayer, and J. Hanan, ''Developmental models of herbaceous plants for computer imagery purposes,'' Comput. Graph. **22**, 141–150 (1988).
[25] K. J. Niklas, ''Computer-simulated plant evolution,'' Sci. Am. **254**, 68–75 (1986).
[26] X. G. Viennot, G. Eyrolles, N. Janey, and D. Arques, ''Combinatorial analysis of ramified patterns and computer imagery of trees,'' Comput. Graph. **23**, 31–40 (1989).
[27] P. Taylor, R. Owens, and D. Ingram, ''Simulated mammography using synthetic 3D breasts,'' in Ref. 22, pp. 283–290.
[28] J. Vannimenus and X. G. Viennot, ''Combinatorial tools for the analysis of ramified patterns,'' J. Stat. Phys. **54**, 1529–1538 (1989).
[29] R. E. Horton, ''Erosional development of systems and their drainage basins: hydrophysical approach to quantitative morphology,'' Bull. Geol. Soc. Am. **56**, 275–370 (1945).
[30] A. N. Strahler, ''Hypsometric (area-altitude) analysis of erosional topography,'' Bull. Geol. Soc. Am. **63**, 1117–1142 (1952).
[31] M. J. Woldenberg, ''A structural taxonomy of spatial hierarchies,'' *Colston Papers* (Butterworths, London, 1970), Vol. 22, pp. 147–175.
[32] J. G. Penaud, ''Matrice de ramification des arbres binaires,'' Discrete Appl. Math. **31**, 1–21 (1991).
[33] A. P. Moskalik, P. L. Carson, and M. A. Rubidoux, ''3D tracking and display of mammary ducts,'' Proceedings of the 1995 IEEE Ultrasonics Symposium, Seattle, WA, 1995, pp. 1167–1170.
[34] A. L. Ames, D. R. Nadeau, and J. L. Moreland, *The VRML Sourcebook* (Wiley, New York, 1996).
[35] Electronic Physics Auxiliary Publication Service, www.aip.org/pubservs/epaps.html, pending.
[36] P. R. Bakic, M. Albert, and A. D. A. Maidment, ''Classification of galactograms using ramification matrices: preliminary results,'' Acad. Radiol. **10**, 198–204 (2003).